Int. J. Electrochem. Sci., 17 **(2022)** Article Number: 220436, doi: 10.20964/2022.04.21

International Journal of
ELECTROCHEMICAL
SCIENCE
www.electrochemsci.org

Hydrothermal Synthesis of $NiCo_2S_4$ Nanotube and Its Investigation as Electrode Material

Junbo Qin, Xinyi Chi, Junjie You[*]*, Chuanqing Du, Yourong Wang and Siqing Cheng*

Innovation Centre for Nanomaterials in Energy and Environment (ICNEE), School of Chemical and Environmental Engineering, Wuhan Polytechnic University, Hubei 430023, P. R. China
[*]E-mail: icnee@whpu.edu.cn

Received: 28 November 2021 / *Accepted:* 24 January 2022 / *Published:* 4 March 2022

$NiCo_2S_4$ nanotubes were fabricated time-dependently and hydrothermally at 180 °C and investigated electrochemically as electrode materials. The results show that the as-synthesized $NiCo_2S_4$ nanotube as anode for lithium ion battery deliver an initial specific capacity of as high as 1780 mAh g^{-1} at the current density of 100 mA g^{-1} with poor cycling stability and rate capacity, indicating the potential pseudocapacitive features of $NiCo_2S_4$ nanotube. Furthermore, the $NiCo_2S_4$ nanotube electrode for supercapacitor demonstrates superior electrochemical performance with superb cycling stability and rate capability, testifying $NiCo_2S_4$ nanotube as pseudocapacitance due to the surface diffusion-controlled mechanism of charge storage. These results enable a promise of $NiCo_2S_4$ nanotube as intercalation pseudocapacitance rather than as anode for lithium ion battery.

Keywords: $NiCo_2S_4$ nanotube; Electrode materials; Lithium ion battery; Pseudocapacitance; Electrochemical performance.

1. INTRODUCTION

With the ever-increasing demand of renewable energy resources and the severe deterioration of environmental issue, rechargeable lithium ion batteries (RLIBs) and supercapacitors have been deemed to be at the forefront of high efficient and sustainable energy storage devices for powering the ubiquitous portable electronics and even electric vehicles in our society due to their remarkable advantages such as environmental friendliness, outstanding power/energy density, high reliability and long cycle lifespan.[1, 2] Based on the charge-storage properties, RLIBs possesses high energy density but relatively low power density whereas supercapacitor can provide superb power density and long cycle life but suffer from relatively low energy density and low capacitance.[3-5] Therefore, the coupling of these devices to be termed pseudocapacitance has been defined and focused as a promising device with high energy density

without sacrificing the power density, cycling stability and cost effectiveness due to their respective advantages complementary to each other.[6-9]

According to the charge-storage mechanism, the electrochemical processes of a pseudocapacitance with similar electrochemical features as those of EDLC (electric double layer capacitor) is that a reversible faradaic charge transfer reaction takes place at or near the surface of an electrode material, offering a much greater capacitive energy storage.[2, 3, 7] As such, it is an unambiguous challenge to find an appropriate material as the pseudocapacitive material for preferably both storing and delivering large amounts of energy. As of now, the most often investigated pseudocapacitive materials are transition metal oxides such as MnO_2, RuO_2, Co_3O_4, $NiCo_2O_4$ and NiO as well as carbides and nitrides due to their glamorous characteristics, whereas some important factors such as the limited energy density, the cost etc. impedes their implementation in practical applications.[10-13] Therefore, substantial efforts have been dedicated to the pseudocapacitive materials with advantages of superior supercapacitive performance and low cost via wise designing and elaborate construction.

In recent years, transition metal sulfides have been widely investigated in diverse electrochemical applications due to their superb theoretical capacity, abundance in nature, good reversibility, low cost and high electrical conductivity.[12-14] Thereinto, ternary nickel cobalt sulfide, $NiCo_2S_4$, have been demonstrated many excellent electrochemical properties as pseudocapacitance exploiting both metal ion contributions in terms of its outstanding intrinsic conductivity, high theoretical specific capacitance, rich redox active sites.[15, 16] Thus, various architectures of $NiCo_2S_4$ were designed and synthesized to maximize the capacitive characteristics, revealing the promise of $NiCo_2S_4$ as the pseudocapacitance.[17-19] The charge-storage mechanism of $NiCo_2S_4$ electrode as pseudocapacitance has been verified to be the rich faradaic redox reaction of Ni^{2+}/Ni^{3+}, Co^{2+}/Co^{3+} and Co^{3+}/Co^{4+} redox couples at or near the surface of $NiCo_2S_4$. Moreover, the reaction kinetics of $NiCo_2S_4$ electrode as pseudocapacitance exhibited the typical pseudocapacitive feature. On the other hand, many investigations [20-22]on $NiCo_2S_4$ as anode material for lithium ion battery were reported recently on basis of the conversion reaction with lithium ion, which appear reasonable from the electrochemical measurements such as galvanostatic charge/discharge test, cyclic voltammogram and AC impedance spectroscopy. Of course, it is believed undoubtedly that an electrode material could act as both battery and capacitor at different situation. However, for $NiCo_2S_4$, it should be worthy of contemplating whether $NiCo_2S_4$ possesses capacitive feature when used as anode materials for lithium ion battery so that it could distinguish the exact choose in practical applications. To our knowledge, no report is available about the in-depth discussion of $NiCo_2S_4$ electrode as lithium ion battery versus supercapacitor.

In this work, the $NiCo_2S_4$ nanotubular structure was fabricated time-dependently and investigated as electrode materials for lithium ion battery and pseudocapacitance, which aims at giving insight into the charge storage underlying mechanism of $NiCo_2S_4$ electrode so as to exert its exact application in the future.

2. EXPERIMENTAL SECTION

2.1 Materials

All chemicals including nickel nitrate hexahydrate ($Ni(NO_3)_2·6H_2O$), Cobalt nitrate hexahydrate ($Co(NO_3)_2·6H_2O$), thiourea ($CO(NH_2)_2$), N-methylpyrrolidone (NMP), potassium hydroxide (KOH), polyvinylidene fluoride (PVDF), hydrochloric acid (HCl) and absolute ethanol etc. were available commercially in analytical grade from Sinopharm Chemical Reagent Co. (Shanghai, China) and were used as received without any further purification unless stated otherwise. Water used in all experiments was distilled and deionized to 16.5 MΩ·cm of electrical resistivity.

2.2 Synthesis of $NiCo_2S_4$ nanotube

$NiCo_2S_4$ nanotube was fabricated time-dependently by a hydrothermal method using $Ni(NO_3)_2·6H_2O$ as nickel resource, $Co(NO_3)_2·6H_2O$ as Co source and thiourea as sulfur source. In a typical run, 1.5 mmol (0.436 g) of $Ni(NO_3)_2·6H_2O$, 3 mmol (0.873 g) of $Co(NO_3)_2·6H_2O$ and 9 mmol (0.685 g) of thiourea were stirred vigorously for at least 30 min and were dissolved in 60 ml of deionized water at room temperature to obtain a light pink transparent solution. Subsequently, the as-prepared solution above was transferred to a Teflon-lined stainless-steel autoclave with a capacity of 100 ml. Then, the Teflon-lined autoclave was sealed and heated to 180 °C and maintained for 48, 96 hours (named as NCS-1, NCS-2), respectively. After being cooled to room temperature naturally, the synthesized products were collected by centrifugation, rinsed several times with distilled water and absolute ethanol and dried in vacuum drying oven at 60 °C overnight.

2.3 Instrumentation and structural characterization

The structures of the as-synthesized $NiCo_2S_4$ were identified by powder X-ray diffraction (PXRD) in a Shimadzu XRD 6000 X-ray diffractometer with Cu Kα source (λ = 1.5418 Å) radiation with an accelerating voltage of 45 kV and the diffraction angle (2θ) range of $10° < 2\theta < 80°$at a scan rate of 4° min^{-1} calibrated against corundum standard. The resultant XRD patterns were indexed to the standard JCPDS file (20-0782) of $NiCo_2S_4$ and the particle size was evaluated approximately at the (311) peak using the Scherrer formula, where the fwhm of the peak was determined by fitting the (311) peak to a pearson VII function using JADE fitting software. The field emission scanning electron microscopy (FESEM) was carried out on a JOEL JSM-6701 to characterize the morphologies of the as-synthesized $NiCo_2S_4$ materials. The transmission electron microscopy (TEM) images and high-resolution transmission electron microscopy (HRTEM) images were observed on a FEI Tecnai G2 F20 at an acceleration voltage of 200 kV to characterize the hollow or porous structure of the as-synthesized $NiCo_2S_4$ materials.

2.4 Electrochemical measurements

Electrochemical measurements were performed on a program-controlled Battery Test system (LAND, Wuhan, China) and a CHI660B electrochemical workstation (Chenghua, Shanghai, China). For battery measurements, the 2032-type coin cells with Celgard® 2325 separator were assembled in an Argon-filled Mikrouna-lab glovebox (H_2O, O_2<0.1 ppm) using the as-prepared $NiCo_2S_4$ nanotube materials as working electrodes, lithium foil as the counter/reference electrode. The used electrolyte was lithium hexafluorophosphate ($LiPF_6$, 1 mol/dm^3) in a 1:1 (v/v) mixed solvent of ethylene carbonate (EC) and diethyl carbonate (DEC). The working electrodes were prepared by the traditional slurry-coating method. In a typical procedure, the as-obtained $NiCo_2S_4$ materials (70 wt%) as active materials, carbon black (CB, 20 wt%) as a conductive agent and polyvinylidene fluoride (PVdF, 10 wt%) as a binder were mixed in N-methyl-2-pyrrolidone (NMP) as solvent under ultrasonic condition to form a homogenous slurry. Subsequently, the resultant slurry was compressed uniformly onto copper foil (1×1 cm^2) current collector and allowed to dry in vacuum oven at 80 °C overnight to generate the working electrodes with the active material areal mass loading of ~ 1.5 mg cm^{-2}. The Galvanostatic charge/discharge (GCD) testing were carried out on the aforementioned battery test system at diverse current densities in the voltage ranging from 0 to 3.0 V vs. Li/Li$^+$. Cyclic voltammetry (CV) profiles were recorded at different sweep rates in the same voltage range as that of the GCD on a CHI660B electrochemical workstation and electrochemical impedance spectroscopy (EIS) was measured in an AC frequency of 100 kHz – 0.01 Hz with a perturbation signal of ± 5 mV on the same workstation. The electrochemical performance of the as-obtained $NiCo_2S_4$ as pseudocapacitor was measured using an open three-electrode cell configuration at room temperature with an aqueous solution of 2 M KOH as electrolyte, a platinum sheet as the counter electrode and a HgO/Hg (SCE) as the reference electrode. The working electrodes mainly consisting of the as-prepared $NiCo_2S_4$ were fabricated by almost the same as the slurry-coating method and the detailed preparing procedure was to mix the as-prepared active material $NiCo_2S_4$, the binder PVdF and the conducting agent CB with the weight ratio of 8:1:1 in the solvent NMP under ultrasonic condition to generate a homogeneous slurry, followed by coating the slurry on foamed nickel (1×1 cm^2) and dried in a vacuum oven at 80 °C for 24 hours, resulting in a working electrode with the active material mass loaded of ~ 5 mg. The electrochemical measurements such as GCD, CV and EIS were conducted all on the same electrochemical workstation as aforementioned. The Galvanostatic charge/discharge (GCD) curves were measured with the potential window from 0 to 0.7 V (versus SCE) at the various constant current density ranging from 1 to 10 A g^{-1}. The cyclic voltammetry (CV) was carried out with the same potential window as GCD tests at different sweep rates varying from 2 to 50 mV s^{-1}. The electrochemical impedance spectroscopy (EIS) plots were recorded in an alternating current frequency ranging from 100 kHz to 0.01 Hz at open circuit potential of 0.25 V with a perturbation signal of 5 mV. The specific capacitances of the electrodes were calculated from the corresponding discharge curves by the following formula:[23-25]

$$C = \frac{I\Delta t}{m\Delta V} \qquad (1)$$

where C is the specific capacitance in F g^{-1}, I is the constant discharging current in A, Δt is the discharge time in s, ΔV is the window potential during the discharge process after the internal resistance (IR) drop (V), and m is the mass of the active electrode material in g.

3. RESULTS AND DISCUSSION

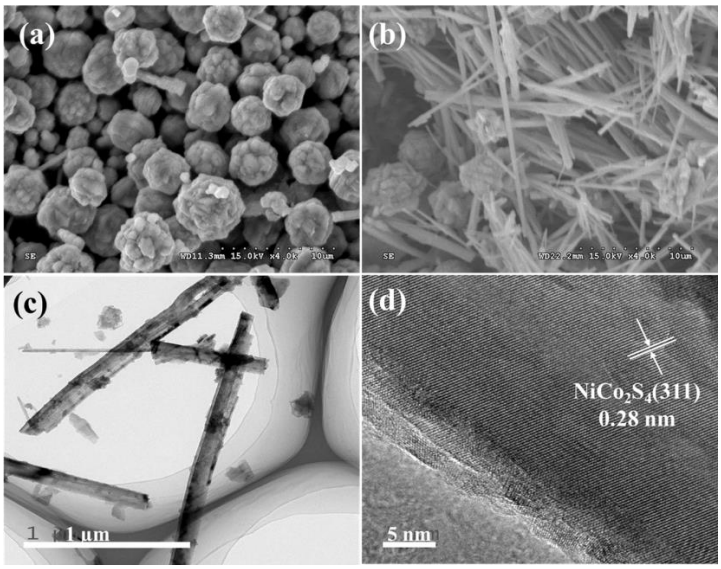

Figure 1. (a-b) SEM images of NCS-1 and NCS-2, respectively, (c) TEM image of NCS-2, (d) HRTEM image of NCS-2.

$NiCo_2S_4$ electrode nanomaterials were fabricated by the traditional hydrothermal method using $Ni(NO_3)_2{\cdot}6H_2O$ as Ni source, $Co(NO_3)_2{\cdot}6H_2O$ as Co source and thiourea as sulfur source at 180 °C for different reaction time. It is found that the as-obtained $NiCo_2S_4$ materials are nano-scale due to the process of nucleus formation and thus nucleus growth by the release of sulfur from the thiourea, which assemble spontaneously into different morphologies with the evolution of reaction time, as presented typically in Fig.1a-b for the reaction time of 48 and 96 hours, respectively. From Fig. 1a-b, it can be seen that $NiCo_2S_4$ nanomaterials assemble themselves into microspherical structure when the reaction proceeds for 48 hours while most of all are nanotubular structure for 96 hours which are beneficial for being acted as electrode material due to the high accessibility of the electrolyte.[26, 27] Thus, the latter $NiCo_2S_4$ nanotubular structure was further characterized by TEM and HRTEM, as shown Fig. 1c-d. It is indicated that the magnitude of porous nanotube is ca. 100 nm in diameter and the HRTEM image of NCS-2 displays lattice fringes spacing of 0.28 nm corresponding to (311) planes of $NiCo_2S_4$, which are in consistent with the calculated results from XRD patterns using Bragg's law[28, 29], as exhibited in Fig. 2 for the further analysis of the composition and purity of the as-synthesized NCS-1 and NCS-2. From Fig.2, those observed diffraction peaks located at 16.34°, 26.83°, 31.59°, 38.32°, 50.46°, 55.33 can be well indexed to the (111), (220), (311), (400), (511) and (440) crystal planes of the cubic spinel $NiCo_2S_4$ phase, respectively (JCPDS card no. 20-0782), without any other crystallized phase peaks to be detected, indicating the high purity of the products, which is almost identical for the XRD patterns of the as-obtained NCS-1 and NCS-2. Nevertheless, the fwhm of the characteristic peak at (311) crystal plane is various apparently, indicating the different particle size constituting the morphology of the as-synthesized products on basis of the Scherrer formula:[9, 30]

$$D = \frac{K\lambda}{B\cos\theta} \qquad (2)$$

where D is the diffraction particle size, K is the Scherrer constant, λ is the wavelength of X-ray, B is the full width at half maximum (fwhm) or the peak integral breadth and θ is the Bragg diffraction angle. Here, K is valued as 0.89 when B is the fwhm. Thus, it could be obtained that the particle sizes of NCS-1 and NCS-2 are 10.2, 8.6 nm, respectively, which is well consistent with TEM results.

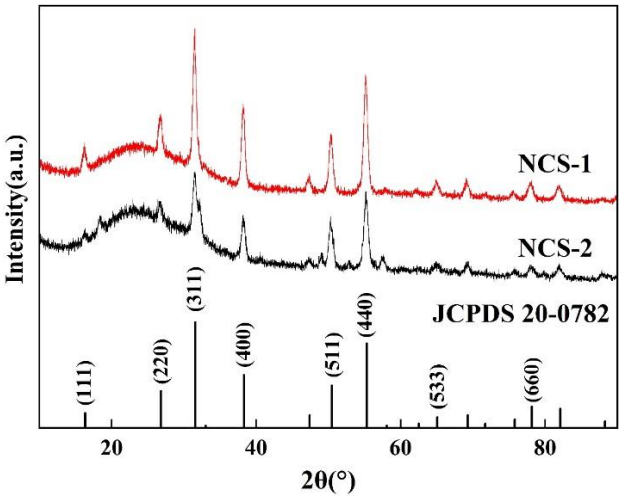

Figure 2. XRD patterns of the as-prepared NCS-1 and NCS-2

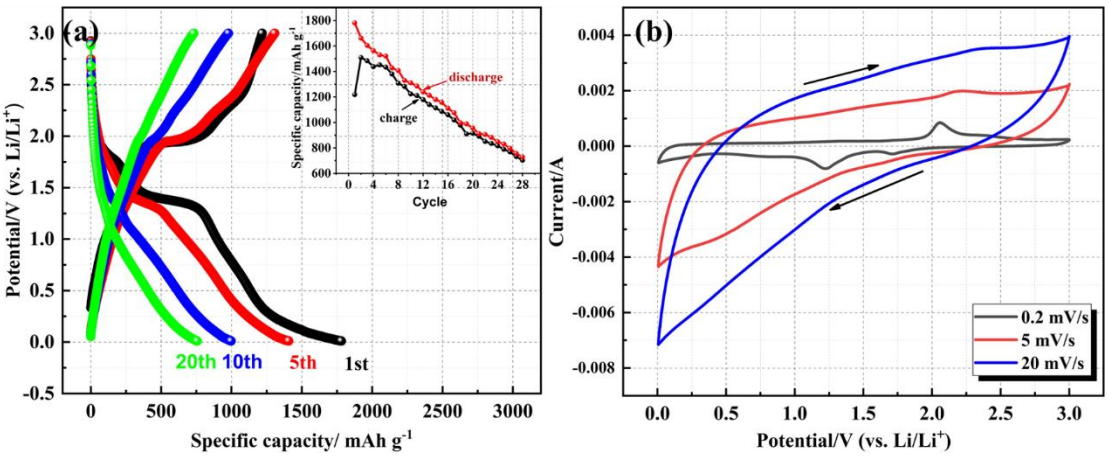

Figure 3. (a) Galvanostatic charge/discharge profiles of the as-obtained NCS-2 electrode as lithium ion battery at the current density of 100 mA g^{-1} at the potential window of 0-3.0 V versus Li/Li^+; The inset shows the cycling stability. (b) CV curves of NCS-2 as lithium ion battery at different sweep rate from 0 to 3.0 V versus Li/Li^+.

As mentioned above, the as-obtained NCS-2 nanotubular structure is more favorable for the transportation and accessibility to active material of electrolyte when used as electrode material. Thus, the as-obtained NCS-2 nanotubular material was used to identify the electrochemical characteristics of $NiCo_2S_4$ electrode as lithium ion battery or supercapacitor by the traditional electrochemical measurements so that we could figure out whether $NiCo_2S_4$ is more suitable for lithium ion battery

electrode or for supercapacitor electrode. Fig. 3a presents the typical cycling galvanostatic charge/discharge (GCD) profiles of NCS-2 electrode as lithium ion battery. From Fig.3a, NCS-2 electrode as lithium ion battery delivers an overwhelmingly high initial discharge and charge specific capacity of 1780 and 1483.5 mAh g^{-1}, respectively at the current density of 100 mA g^{-1} with the discharge flat voltage of around 1.30 V due to the reduction of $NiCo_2S_4$ to generate the metallic Ni and Co, and the charge flat voltage of around 1.96 V owing to the oxidation of Co and Ni to form Co^{2+} and Ni^{2+}, illustrating the typical lithiation and delithiation behavior in the initial charge/discharge process of $NiCo_2S_4$ as lithium ion battery electrode.[31-33] Nonetheless, the flat voltages in the charge/discharge curves gradually become vague and even disappears with the proceeding cycle, and the specific discharge/charge capacity also drop rapidly, demonstrating the transition of kinetic behavior from diffusion-controlled insertion of Li^+ because of the redox reaction of NCS-2 to the adsorption of Li^+ onto the surface of NCS-2. Thus, the cycling stability of NCS-2 electrode as lithium ion battery could not be fine, as shown in the inset of Fig.3a for the poor cycling stability and coulombic efficiency. This is manifested further by the CV curves of NCS-2 electrode as lithium ion battery in Fig. 3b. From Fig. 3b, at a slow sweep rate of 0.2 mV s^{-1}, the visible cathode peak at ca. 1.30 V and anode peak at ca. 1.96 V are observed, which is in agreement with the initial galvanostatic charge/discharge profile with charge/discharge flat voltage[34-36], featuring further the electrochemical behavior of NCS-2 during the lithiation/delithiation process. Notwithstanding, with increasing the sweep rate, the characteristic redox peak plateau at CV curves fade away and the cyclic voltammograms tend to be a similar rectangle, which is the property of the classic electric double-layer capacitors (EDLCs) and thus corroborate the linear charge/discharge curves for prolonged cycles in Fig. 3a. Therefore, the as-obtained NCS-2 tubular structure might be regarded critically as pseudocapacitor materials rather than lithium ion battery materials since the capacitive feature is demonstrated as well even if used as anode materials for lithium ion battery.

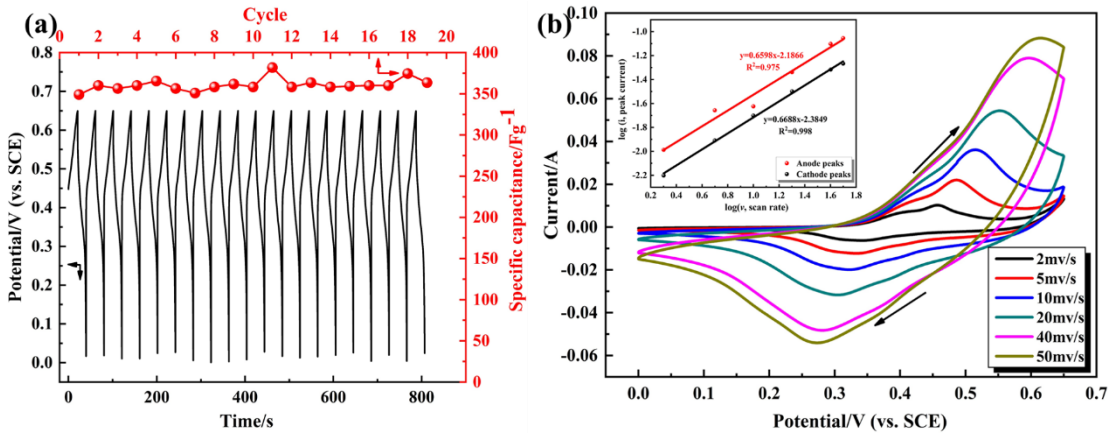

Figure 4. (a) Galvanostatic charge/discharge curves at the continuous cycles and cycling stability of the as-obtained NCS-2 electrode as supercapacitor at the current density of 10 A g^{-1} at the potential window between 0 and 0.65 V versus SCE. (b) CV curves of NCS-2 at different sweep rate as supercapacitor from 0 to 0.65 V versus SCE, the inset shows the log(*i*) *vs.* log(*v*) plots at the redox peaks of NCS-2 electrode.

To illustrate the electrochemical performance of NCS-2 electrode as supercapacitor, the three-electrode system with platinum as counter electrode and SCE as reference electrode was employed in 2 M KOH electrolyte solution to conduct the galvanostatic charge/discharge (GCD) and CV test, as presented in Fig. 4. From Fig. 4a, it can be seen that the GCD curves exhibit the obvious plateau regions, indicating the pseudocapacitive feature of NCS-2 electrode, and the calculated specific capacitance at the current density of 10 A g^{-1} based on the eqn.(1) is about 350 F g^{-1} with 3% decay after 20 cycles, exhibiting a excellent cycling stability, which is remarkably different from NCS-2 electrode as lithium ion battery. In order to further demonstrate the kinetic behavior of NCS-2 electrode as pseudocapacitor, CV test was conducted using the three-electrode system at different sweep rates ranging from 2 to 50 mV s^{-1} at the potential window of 0-0.65 V versus SCE, as presented in Fig.4b. Evidently, with increasing the sweep rates from 2 to 50 mV s^{-1}, the reduction peaks shift towards the low potential while the oxidation peaks shift towards the high potential owing to the polarization of NCS-2 electrode. Meanwhile, the shapes of all CV curves are almost identical with increasing the sweep rates from 2 to 50 mV s^{-1}, indicative of outstanding rate performance of NCS-2 electrode. Furthermore, all CV curves appear the visible faradaic redox peaks within the investigated potential window due to the reversible Faradaic redox reaction of Co^{3+}/Co^{4+}, Ni^{2+}/Ni^{3+}, and Co^{2+}/Co^{3+} redox couples, which might be modulated by the OH^- ions in a KOH alkaline aqueous solution[37-39], implying the pseudocapacitive characteristics of NCS-2 electrode as capacitor, which match well with the GCD curves. To further illustrate the mechanism of the charge storage mechanism of the as-obtained NCS-2, Dunn's method about the relationship of peak current in CV curves with the sweep rates is employed to explore the capacitive features, which obeys the following eqn.(3) [2, 3]

$$i = av^b \qquad (3)$$

where a and b are the adjustable parameters, i and v are the peak current and the sweep rate, respectively. b value is generally used to judge the charge storage mechanism in which a b-value of 0.5 indicates a semi-infinite diffusion-controlled charge storage while a b-value of 1 show a surface-controlled one.

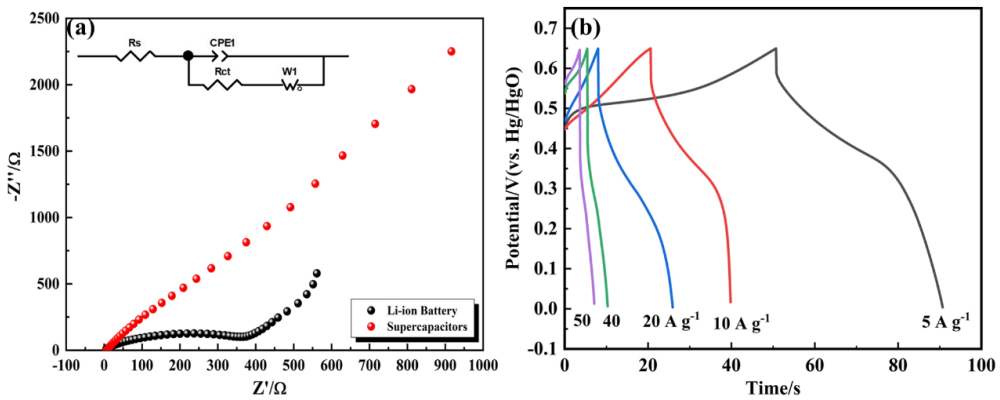

Figure 5. (a) Nyquist plots of NCS-2 electrode as lithium ion battery or supercapacitor at an open circuit voltage of 0.2 V at the AC frequency range of 100 kHz-0.01 Hz, the inset shows the electrical equivalent circuit used for fitting impedance spectra; (b) Galvanostatic charge/discharge profiles of NCS-2 electrode as supercapacitor at different current density at the potential ranging from 0 to 0.65 V versus SCE.

As shown in the inset of Fig.4b for the relationship of anodic (cathodic) peak current with the sweep rate, it is demonstrated that the b-values of the anodic and cathodic peak are 0.6598 and 0.6688, respectively, indicating the combination of both semi-infinite diffusion-controlled and surface-controlled charge storage mechanism of NSC-2 electrode, which manifests further the pseudocapacitive characteristics of NSC-2.

To further get insight into the electrochemical performance of NCS-2, the electrochemical impedance spectroscopy (EIS) was resorted and conducted in the frequency ranging from 100 kHz to 0.01 Hz. The resultant comparative Nyquist plots of NCS-2 electrode as lithium ion battery and pseudocapacitance were presented in Fig. 5a.[40-43] Comparing the Nyquist plot of NSC-2 as lithium ion battery with that as pseudocapacitance, both R_s for the electrolyte resistance corresponding to the intersecting point with the real axis in the higher frequency are low, which is related to the good conductivity of $NiCo_2S_4$ while R_{ct} for the faradaic charge transfer resistance of NCS-2 as lithium ion battery is obviously distinct from and even much higher than that as pseudocapacitance, indicating the capacitive-favorable characteristic controlled by surface charge storage. Notably, the Warburg resistance (Z_w) corresponding to the vertical line in the low frequency region could distinguish the capacitive characteristic of NSC-2 as lithium ion battery because the straight line almost parallels the imaginary impedance axis in the Nyquist plots, which demonstrates the faster ion diffusion and more ideal capacitive features of NCS-2 when used as anode for lithium ion battery, confirming the more favorable capacitive tendency of NCS-2.

Finally, the rate capability of NCS-2 as pseducapacitor was evaluated by the galvanostatic charge/discharge measurements at various current density at the potential windows of 0 – 0.65 V versus SCE so that it can better show NSC-2 to be potential as electrode material for pseudocapacitance. As shown in Fig. 5b, the calculated specific capacitances of NCS-2 as pseudocapacitance by eqn. (1) at the current density of 5, 10, 20, 40, 50 A g^{-1} are 450, 350, 335, 318 and 309 F g^{-1}, respectively, demonstrating the 68.7% retention of the specific capacitance at the current density from 5 to 50 A g^{-1}, which is indicative of better rate capability. This definitely corroborates the potential pseudocapacitive characteristics of NSC-2 as supercapacitor.[44, 45]

4. CONCLUSION

In conclusion, $NiCo_2S_4$ nanotubes with ca. 100 nm in diameter were successfully assembled time-dependently by hydrothermal method. When used as anode for lithium ion battery, the as-obtained $NiCo_2S_4$ nanotube demonstrates poor cycling stability and rate capability even through it could deliver an overwhelming initial specific discharge capacity of as high as 1780 mAh g^{-1} at the current density of 100 mA g^{-1} due to the substantial transition of charge storage mechanism from semi-infinite controlled diffusion to surface diffusion with cycling, exhibiting the potential pseudocapacitive characteristics of $NiCo_2S_4$ nanotube. Thus, when used as electrode for pseudocapacitance, the as-obtained $NiCo_2S_4$ nanotube exhibits superb capacitive features with high specific discharge capacitance of 350 F g^{-1} at the current density of 10 A g^{-1}, superior cycling stability and good rate capability due to the rich redox active sites and ultrahigh intrinsic conductivity, further testifying the ideal pseudocapacitive features of

$NiCo_2S_4$ nanotube. Therefore, it is of significance to show $NiCo_2S_4$ as the promise of pseudocapacitive material rather than anode material for lithium ion battery.

ACKNOWLEDGEMENTS
The work was supported by Research and Innovation Initiatives of WHPU (no.2019Y13).

References

1. V. Augustyn, J. Come, M. A. Lowe, J. W. Kim, P. L. Taberna, S. H. Tolbert, H. D. Abruna, P. Simon and B. Dunn. *Nat. Mater.*, 12 (2013) 518.
2. C. Costentin, T. R. Porter and J. M. Saveant. *ACS Appl. Mater. Inter.*, 9 (2017) 8649.
3. P. Simon, Y. Gogotsi and B. Dunn. *Science*, 343 (2014) 1210.
4. M. Wu, Y. Cui, A. Bhargav, Y. Losovyj, A. Siegel, M. Agarwal, Y. Ma and Y. Fu. *Angew. Chem. Int. Ed.*, 55 (2016) 10027.
5. G. Zhou, L. Xu, G. Hu, L. Mai and Y. Cui. *Chem. Rev.*, 119 (2019) 11042.
6. A. C. Forse, J. M. Griffin, C. Merlet, J. Carretero-Gonzalez, A. R. O. Raji, N. M. Trease and C. P. Grey. *Nat. Energy*, 2 (2017) 16216.
7. C. Liu, X. Wu and B. Wang. *Chem. Eng. J.*, 392 (2020) 123651.
8. T. Y. Wei, C. H. Chen, H. C. Chien, S. Y. Lu and C. C. Hu. *Adv. Mater.*, 22 (2010) 347.
9. M. Zhou, Y. Xu and Y. Lei. *Nano Today*, 20 (2018) 33.
10. V. Augustyn, P. Simon and B. Dunn. *Energ. Environ. Sci.*, 7 (2014) 1597.
11. T. Brezesinski, J. Wang, S. H. Tolbert and B. Dunn. *Nat. Mater.*, 9 (2010) 146.
12. X. Chen, Q. Liu, T. Bai, W. Wang, F. He and M. Ye. *Chem. Eng. J.*, 409 (2021) 127237.
13. W. Cheng, H. Di, Z. Shi and D. Zhang. *J. Alloys Compd.*, 831 (2020) 154607.
14. P. Kulkarni, S. K. Nataraj, R. G. Balakrishna, D. H. Nagaraju and M. V. Reddy. *J. Mater. Chem. A*, 5 (2017) 22040.
15. T. Chen, S. Wei and Z. Wang. *ChemPlusChem*, 85 (2019) 43.
16. Y. P. Gao and K. J. Huang. *Chem. Asian J.*, 12 (2017) 1969.
17. X. Gao, Q. Chang, J. Hong, D. Long, G. Jin and X. Xiao. *ChemistrySelect*, 3 (2018) 13751.
18. K. Liang, W. He, X. Deng, H. Ma and X. Xu. *J. Alloys Compd.*, 735 (2018) 1395.
19. Z. Sun, C. Zhao, X. Cao, K. Zeng, Z. Ma, Y. Hu, J.-H. Tian and R. Yang. *Electrochim. Acta*, 338 (2020) 135900.
20. D. Bhattacharjya, A. Sinhamahapatra, J. J. Ko and J. S. Yu. *Chem. Commun.*, 51 (2015) 13350.
21. H. Chen, X. Ma and P. K. Shen. *Chem. Eng. J.*, 364 (2019) 167.
22. B. Guan, S.-Y. Qi, Y. Li, T. Sun, Y.-G. Liu and T.-F. Yi. *J. Energy Chem.*, 54 (2021) 680.
23. W.-W. Liu, C. Lu, K. Liang and B. K. Tay. *J. Mater. Chem. A*, 2 (2014) 5100.
24. R. Sahoo, A. Pal and T. Pal. *Chem. Commun.*, 52 (2016) 13528.
25. J. Yang, Y. Zhang, C. Sun, G. Guo, W. Sun, W. Huang, Q. Yan and X. Dong. *J. Mater. Chem. A*, 3 (2015) 11462.
26. T.-F. Yi, J.-J. Pan, T.-T. Wei, Y. Li and G. Cao. *Nano Today*, 33 (2020) 100894.
27. X. Y. Yu and X. W. Lou. *Adv. Energy Mater.*, 8 (2018) 1701592
28. W. Zhang, J. Chen, Y. Liu, S. Liu, X. Li, K. Yang and L. Li. *J. Alloys Compd.*, 823 (2020) 153631.
29. M. Y. Zhao, L. Zhu, B. W. Fu, S. H. Jiang, Y. N. Zhou and Y. Song. *Acta Phys. Chim. Sin.*, 35 (2019) 193.
30. X. Zuo, Y. Song and M. Zhen. *Appl. Surf. Sci.*, 500 (2020) 144000.
31. D. J. Yu, Y. F. Yuan, D. Zhang, S. M. Yin, J. X. Lin, Z. Rong, J. L. Yang, Y. B. Chen and S. Y. Guo. *Electrochim. Acta*, 198 (2016) 280.

32. H. Zhang, J. Liu, X. Lin, T. Han, M. Cheng, J. Long and J. Li. *J. Alloys Compd.*, 817 (2020) 153293.
33. L. Zhang, Q. Wang, H. Jiu, C. Xie and S. Zhang. *Micro Nano Lett.*, 13 (2018) 993.
34. S. Raj, Y. Dong, P. Kar, L. Mai, S. Jin and P. Roy. *ChemistrySelect*, 3 (2018) 2315.
35. Y. Tao, L. Ruiyi, Z. Lin, M. Chenyang and L. Zaijun. *Electrochim. Acta*, 176 (2015) 1153.
36. J.-G. Wang, D. Jin, R. Zhou, C. Shen, K. Xie and B. Wei. *J. Power Sources*, 306 (2016) 100.
37. S. Peng, L. Li, C. Li, H. Tan, R. Cai, H. Yu, S. Mhaisalkar, M. Srinivasan, S. Ramakrishna and Q. Yan. *Chem. Commun.*, 49 (2013) 10178.
38. K. A. Pettigrew, J. W. Long, E. E. Carpenter, C. C. Baker, J. C. Lytle, C. N. Chervin, M. S. Logan, R. M. Stroud and D. R. Rolison. *ACS Nano*, 2 (2008) 784.
39. C. Prehal, C. Koczwara, N. Jackel, A. Schreiber, M. Burian, H. Amenitsch, M. A. Hartmann, V. Presser and O. Paris. *Nat. Energy*, 2 (2017) 16215.
40. J. Huang, D. Liu, C. Gu and J. Liu. *Mater. Res. Lett.*, 6 (2018) 307.
41. W. Kong, C. Lu, W. Zhang, J. Pu and Z. Wang. *J. Mater. Chem. A*, 3 (2015) 12452.
42. S. Li, P. Xu, M. K. Aslam, C. Chen, A. Rashid, G. Wang, L. Zhang and B. Mao. *Energy Stor. Mater.*, 27 (2020) 51.
43. W. Li, B. Zhang, R. Lin, S. Ho-Kimura, G. He, X. Zhou, J. Hu and I. P. Parkin. *Adv. Funct. Mater.*, 28 (2018) 1705937.
44. H. Chen, J. Jiang, L. Zhang, D. Xia, Y. Zhao, D. Guo, T. Qi and H. Wan. *J. Power Sources*, 254 (2014) 249.
45. B. Liu, D. Kong, Y. Wang, Y. V. Lim, S. Huang and H. Y. Yang. *FlatChem*, 10 (2018) 14.